Archives of Biochemistry and Biophysics 762 (2024) 110204

Contents lists available at ScienceDirect

Archives of Biochemistry and Biophysics

journal homepage: www.elsevier.com/locate/yabbi

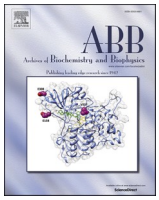

New insights into the function and molecular mechanisms of Ferredoxin-NADP$^+$ reductase from *Brucella ovis*

Andrea Moreno [a,b,c], Isabel Quereda-Moraleda [d], Celia Lozano-Vallhonrat [d], María Buñuel-Escudero [a], Sabine Botha [e], Christopher Kupitz [f], Stella Lisova [f], Ray Sierra [f], Valerio Mariani [f], Pamela Schleissner [f], Leland B. Gee [f], Katerina Dörner [g], Christina Schmidt [g], Huijong Han [g], Marco Kloos [g], Peter Smyth [g], Joana Valerio [g], Joachim Schulz [g], Raphael de Wijn [g], Diogo V.M. Melo [g], Adam Round [g], Fabian Trost [g], Egor Sobolev [g], E. Juncheng [g], Marcin Sikorski [g], Richard Bean [g], Marta Martínez-Júlvez [a,b,**], Jose Manuel Martin-Garcia [d,*], Milagros Medina [a,b,***]

[a] *Departamento de Bioquímica y Biología Molecular y Celular, Facultad de Ciencias, Universidad de Zaragoza, 50009 Zaragoza, Spain*
[b] *Instituto de Biocomputación y Física de Sistemas Complejos (BIFI), and GBsC (Unizar) join Unit to CSIC, Universidad de Zaragoza, 50018 Zaragoza, Spain*
[c] *Departamento de Biología, Facultad de Ciencias, Universidad de los Andes, Venezuela*
[d] *Department of Crystallography and Structural Biology, Institute of Physical Chemistry Blas Cabrera, Spanish National Research Council (CSIC), Madrid, Spain*
[e] *Biodesign Center for Applied Structural Discovery, Arizona State University, Tempe, USA*
[f] *LCLS, SLAC National Accelerator Laboratory, Menlo Park, CA, USA*
[g] *European XFEL, Schenefeld, Germany*

ARTICLE INFO

Handling Editor: J.P. Jin

Keywords:
Ferredoxin-NADP$^+$ reductase
Ferredoxin partner
Electron transfer
Room temperature
X-ray diffraction
Serial femtosecond crystallography
XFEL
Microcrystals

ABSTRACT

Bacterial ferredoxin(flavodoxin)-NADP$^+$ reductases (FPR) primarily catalyze the transfer of reducing equivalents from NADPH to ferredoxin (or flavodoxin) to provide low potential reducing equivalents for the oxidoreductive metabolism. In addition, they can be implicated in regulating reactive oxygen species levels. Here we assess the functionality of FPR from *B. ovis* to understand its potential roles in the bacteria physiology. We prove that this FPR is active with the endogenous [2Fe–2S] Fdx ferredoxin, exhibiting a K_M^{Fdx} in the low micromolar range. At the molecular level, this study provides with the first structures of an FPR at room temperature obtained by serial femtosecond crystallography, envisaging increase in flexibility at both the adenine nucleotide moiety of FAD and the C-terminal tail. The produced microcrystals are in addition suitable for future mix-and-inject time-resolved studies with the NADP$^+$/H coenzyme either at synchrotrons or XFELs. Furthermore, the study also predicts the ability of FPR to simultaneously interact with Fdx and NADP$^+$/H.

1. Introduction

Plant-type Ferredoxin-NADP(H) reductases (EC 1.18.1.2) are FAD-dependent enzymes catalyzing the reversible electron transfer (ET) between the hydride exchanger NADPH and the single electron carrier ferredoxin/flavodoxin (Fd/Fld) [1–5]. This family is divided into plastidic type ferredoxin-NADP$^+$ reductases (herein FNR) and bacterial type ferredoxin(flavodoxin)-NADP$^+$ reductases (herein FPR). FNRs are found in plants and cyanobacteria where they primarily utilize electrons from photosystem I, via Fd or Fld, to generate and store reducing power in the form of NADPH [1,2,4,6]. In contrast, FPRs typically catalyze the reverse, transferring reducing equivalents from NADPH to Fd (or Fld) to provide low-potential reducing power for the bacterial oxidoreductive metabolism [1,4,6–11].

FNRs and FPRs consist of two distinct domains: The N-terminal domain, which accommodates the FAD cofactor, and the C-terminal domain, responsible for binding the pyridine nucleotide coenzyme. However, they show differences in the FAD conformation and

* Corresponding author.
** Corresponding author. Departamento de Bioquímica y Biología Molecular y Celular, Facultad de Ciencias, Universidad de Zaragoza, 50009 Zaragoza, Spain.
*** Corresponding author. Departamento de Bioquímica y Biología Molecular y Celular, Facultad de Ciencias, Universidad de Zaragoza, 50009 Zaragoza, Spain.
E-mail addresses: mmartine@unizar.es (M. Martínez-Júlvez), jmmartin@iqf.csic.es (J.M. Martin-Garcia), mmedina@unizar.es (M. Medina).

https://doi.org/10.1016/j.abb.2024.110204
Received 6 October 2024; Received in revised form 30 October 2024; Accepted 31 October 2024
Available online 8 November 2024

environment [1,2,6,10,12–17]. In FNRs, the FAD shows an L-shaped extended conformation, with the pyrophosphate (PPi) group acting as a hinge and the adenosine moiety being bound to a flexible sheet–loop–sheet motif. In addition, in FNRs the isoalloxazine stacks between two tyrosine residues, being the tyrosine located at the *re*-face of the ring the C-terminal residue [1,2,6,10,17,18]. However, in FPRs the FAD adenine nucleotide moiety folds back towards the isoalloxazine [6,10,15,17,19–21]. Moreover, FPRs have a C-terminal extension (known as C-terminal tail) and the residue facing the *re*-face of the isoalloxazine is not the C-terminal. The length and sequence of this extension differentiates FPRs into two subclasses. In subclass I, an alanine residue stacks at the *re*-face of the isoalloxazine, followed by a phenylalanine and up to five additional residues. In subclass II, a tyrosine residue stacks against the *re*-face of the isoalloxazine, followed by a tryptophan. In both cases, the aforementioned Phe or Trp at the C-terminal tail are stacked on top of the adenosine moiety of FAD, apparently contributing to its folded conformation. These structural differences have been related to FNRs showing, in general, higher efficiencies than FPRs in the overall ET process, likely due to the requirements of the *in vivo* specific physiological processes they are involved in ([18]. In general, less is known about the FPR functions and mechanisms when comparing to FNRs, but structural differences between them are thought to be a consequence of divergence achieved along functional specialization.

Brucella ovis, the causative agent of ovine brucellosis, encodes an FPR as well as two Fds as potential electron acceptors [22]. One of these Fds is expected to contain a [2Fe2S] cluster (named Fdx), while the other is predicted to hold one [3Fe4S] and one [4Fe4S] cluster (FdA). By similarity with others, FPR from *B. ovis* was proposed to deliver electrons from NADPH to the redox-based metabolism and/or to oxidize NADPH to regulate the *soxRS* regulon that protects bacteria against the host oxidative response during infection. In a previous study, we reported that this FPR efficiently oxidizes NADPH [23]. Cryogenic crystal structures for the oxidized FPR, both in its free form (herein cryo-FPR_{ox}) and in complex with $NADP^+$ (herein cryo-FPR_{ox}:$NADP^+$), revealed minimal structural differences and confirmed it belongs to subclass I (Fig. S1) [23]. In addition, the structure of the FPR_{ox}:$NADP^+$ complex (Fig. S1B), despite binding the 2′P-AMP moiety of $NADP^+$ at the expected site, shows the redox-reactive nicotinamide nucleotide (NMN) portion of the coenzyme in a non-competent orientation for hydride transfer (HT). In fact, in this structure, as well as in those reported for other FPRs in complex with the coenzyme [10,23,24] and PDB ID 5THX (unpublished), the adenine moiety of FAD and the C-terminal tail prevent approaching of the NMN of the coenzyme to the isoalloxazine ring of FAD. However, pre-steady-state kinetics in solution revealed the formation of two charge-transfer complexes, corresponding to the FPR_{ox}:NADPH and the FPR_{rd}:$NADP^+$ species [23], confirming that during catalysis the nicotinamide and flavin reacting rings stack to facilitate HT. These studies also identified the HT itself as the rate limiting step in the reductive half reaction of FPR [23]. Moreover, the C-terminal tail of FPR and the folded conformation of the FAD are expected to play a key role in this process, with the adenine of the cofactor as the element to position the reactive atoms in conformations competent for HT.

This study investigates the role of FPR from *B. ovis*, focusing on its potential roles as an electron donor and in the structural aspects of the catalytic reaction. We prove that FPR shows activity with the endogenous *B. ovis* [2Fe–2S] Fdx. In addition, we provide the first structures of FPR_{ox} at room temperature obtained by serial femtosecond crystallography. Our room temperature structures display an increase in flexibility at both the adenine nucleotide moiety of FAD and the C-terminal tail. Finally, we also predict the ability of FPR to simultaneously interact with $NADP^+$/H and Fdx.

2. Materials and methods

2.1. Expression and purification of FPR and Fdx

Recombinant FPR from *B. ovis* was expressed and purified from *Escherichia coli* cultures as previously reported and stored in 25 mM Tris/HCl, pH 7.4 [23]. To produce Fdx from *B. ovis*, the sequence of the gene encoding it (ENA|ABQ60274|ABQ60274.1 *Brucella ovis* ATCC 25840 ferredoxin, 2Fe–2S) was cloned into pET28a(+) vector (GenScript) as a recombinant His_6-fusion protein with a LEVLFQGP cleavage site for the PreScission Protease. *E. coli* Rosetta™(DE3) competent cells were transformed with the pET28a(+)-Fdx plasmid. Transformed colonies, grown on agar plates, were used to inoculate a starter culture in Luria-Bertani (LB) media supplemented with kanamycin (30 μg/ml). This culture was incubated overnight at 37 °C and 180 rpm. Next day, it was diluted 1:50 in 1 L of LB media, supplemented with kanamycin (30 μg/ml), and incubated at 37 °C and at 180 rpm. When the optical density at 600 nm (OD_{600}) was 0.8, Fdx expression was induced with 0.2 mM isopropyl β-D-1-thiogalactopyranoside, and supplemented with a ferrous sulphate chelate solution 100x (Sigma). Cells were further grown at 30 °C, with orbital shaking at 180 rpm overnight, then harvested by centrifugation at 5000×*g* at 4 °C, and then stored at −20 °C. Frozen cells were thawed in lysis buffer (20 mM Tris/HCl, pH 8.0, 300 mM NaCl, 10 % glycerol, and Triton X-100) supplemented with the protease inhibitor cocktail cOmplete EDTA free (Roche), 1.0 mg/ml lysozyme, 20 μg/ml DNAase I (Sigma), and 4.5 mM $MgSO_4$. The mixture was incubated for 1h and subsequently sonicated in a DRH UP200 DR sonicator (Hielscher) for 10 cycles of 30 s, with 80 % amplitude and 0.5 s pulses, each followed by resting periods of 60 s, in an ice bath. The cell debris was removed by centrifugation at 40 000×*g* at 4 °C for 45 min. The purification protocol for Fdx was adapted from those previously reported for similar proteins [25]. The first purification step was performed on a His-Trap™ column (Cytiva) connected to the ÄKTA™ system (Cytiva) using a 50–300 mM imidazole gradient in 20 mM Tris/HCl, pH 8.0, 300 mM NaCl. The fractions containing the His_6-tagged Fdx were pooled, and the His_6-tag was cleaved from Fdx using PreScission Protease at a 1:5 protease-to-Fdx mass ratio (mg). The cleavage was performed during extensive overnight dialysis at 4 °C in 20 mM Tris/HCl, 150 mM NaCl, pH 8.0. The solution was passed through two columns in tandem, a GST-trap™ and a His-trap™ (Cytiva), connected to the ÄKTA™ system (Cytiva) to respectively bind the protease and the remaining un-cleaved His_6-tagged Fdx in 20 mM Tris/HCl, 150 mM NaCl, pH 8.0. Fdx was obtained in the flow-through fraction after passing the tandem columns. This sample was concentrated using 10 kDa Merck Amicon™ ultrafiltration devices (Millipore) and further purified with size exclusion chromatography (SEC) using a Superdex® Increase 75 10/300 GL (Cytiva) column previously equilibrated in 20 mM Tris/HCl, 150 mM NaCl, pH 7.5. In comparison with the native form, the Fdx purified in this study contained four additional amino acids (GPSH) at the N-terminus.

For both FPR and Fdx, detection during purification and purity were assessed by 15 % SDS–PAGE. Pure proteins were stored at −20 °C until use. Protein and NADPH concentrations were determined by absorption spectroscopy using the following extinction coefficients: FPR_{ox}, ε_{451nm} = 11.5 mM^{-1} cm^{-1} [23]; Fdx_{ox}, ε_{423nm} = 7.2 mM^{-1} cm^{-1} [26] and NADPH (Sigma-Aldrich), ε_{340nm} = 6.22 mM^{-1} cm^{-1}. The correct assembly of the Fdx iron-sulphur cluster was evaluated by determining the A_{340}/A_{280}, A_{412}/A_{280}, and A_{456}/A_{280} ratios [25,27].

2.2. Steady-state enzymatic assays

The FNR-dependent NADPH cytochrome *c* reductase activity was used to establish the Fdx ability to accept electrons from FPR, as well as to evaluate the corresponding FPR steady-state kinetic parameters [28]. Standard reaction mixtures contained 10 nM FPR_{ox}, 0.75 mM cytochrome *c* (Sigma), and varied concentrations of NADPH or Fdx. The cytochrome *c* reduction by Fdx was monitored spectrophotometrically

at 550 nm using 20 mM^{-1} cm^{-1} as the extinction coefficient of change for cytochrome *c* reduction [29]. Measurements were carried out at 25 °C in 50 mM Tris/HCl, pH 8.0. k_{cat} and K_m^{Fdx} values were calculated by data fitting to the Michaelis-Menten equation using Origin 2024.

2.3. Production and optimization of FPR_{ox} microcrystals

Initial micro-crystallization tests were conducted using both the batch and the free interface diffusion (FID) methods [30]. These tests involved evaluating various precipitant buffer compositions, protein-to-precipitant ratios (1:1, 1:2, and 1:3), and different protein concentrations (16 and 22 mg/mL) (Table S1). The precipitant buffers used in the micro-crystallization trials were formulated based on established crystallization conditions known to produce large crystals [23]. Best FPR_{ox} microcrystals were obtained by the batch method with a precipitant of the following composition: 25 % PEG 4000, 0.1 M MES pH 6.5, 0.2 M $MgCl_2$, using a 1:2 protein to precipitant ratio and a protein concentration of 22 mg/mL (Fig. 1A). We employed seeding techniques to improve the homogeneity and quantity of crystalline samples for measurements at the Linac Coherent Light Source (LCLS) at the SLAC National Accelerator Laboratory (Menlo Park, USA) and European XFEL (EuXFEL) (Hamburg, Germany) facilities. Using the previously described crystallization conditions, we added 1 μL of crystal seeds to 100 μL of precipitant buffer and then repeated the batch experiment. The seeds were prepared by crushing previously obtained crystals with glass beads (Fig. 1B). After 24 h, rod-shaped crystals with an average length of 25–35 μm in their longest dimension were produced (Fig. 1C, D and 1E).

2.4. Serial data collection on FPR_{ox} microcrystals at LCLS and the EuXFEL

Serial room temperature data collection on FPR_{ox} microcrystals was performed at two XFEL facilities, the MFX instrument [31] of the LCLS during protein crystal screening beamtime P10027 and the SPB/SFX instrument of the EuXFEL during the protein crystal screening proposal ID P5458. In both experiments, pure FPR_{ox} protein was shipped to the XFEL facility and FPR_{ox} microcrystals were obtained on site as described in *section 2.4*. The microcrystal suspension was filtered before injection using a 20 μm mesh filter to break up large crystals aggregates and to avoid clogging problems while injecting the sample. The experimental setup used in these experiments is shown in Fig. 2A. At the LCLS, SFX data were collected using the microfluidic electrokinetic sample holder (MESH) injector [32] at a flow rate of 3 μL/min (Fig. 2B). Diffraction snapshots were collected on the ePix10k-2M [33] detector at a repetition rate of 120 Hz and X-ray energy of 11.2 keV using a pulse duration of 40 fs. The sample to detector distance was set to 135 mm. A customized version of OnDA (Online Data Analysis) Monitor called OM, was used for live feedback of crystal hit rates [34]. At the EuXFEL, data collection was performed initially with the double flow focusing nozzle (DFFN) [35,36] (Fig. 2C) with the following settings: sample at 20 μL/min, ethanol at 20 μL/min, and helium at 18–22 mg/min. However, due to nozzle clogging, we switched to C-type GDVN [36] for the remainder of the reservoir, adjusting the settings to 40–50 μL/min for the sample and 33 mg/min for helium. Diffraction snapshots were collected on the AGIPD 1 Mpx detector [37] at a repetition rate of 1.1 MHz with the DFFN and 0.5 MHz with the C-type GDVN, and X-ray energy of 9.4 keV using a pulse duration of 25 fs. The sample-to-detector distance was set to 122 mm. All data collection statistics are listed in Table 1.

2.5. Data processing and structure determination of FPR

Data processing was carried out off-site after the experiments. For LCLS data, crystal hits were initially identified using the Cheetah software [38] following gain calibration. A crystal hit was defined based on specific criteria: Peakfinder 8 was used with an ADC threshold of 50, a minimum SNR of 5, and a minimum of one pixel per peak to identify at least 10 peaks within a resolution range of 0–700 pixels. Hits were then indexed using CrystFEL software (version 0.10.2) [39,40]. Indexing attempts were conducted with algorithms including MOSFLM [41] and

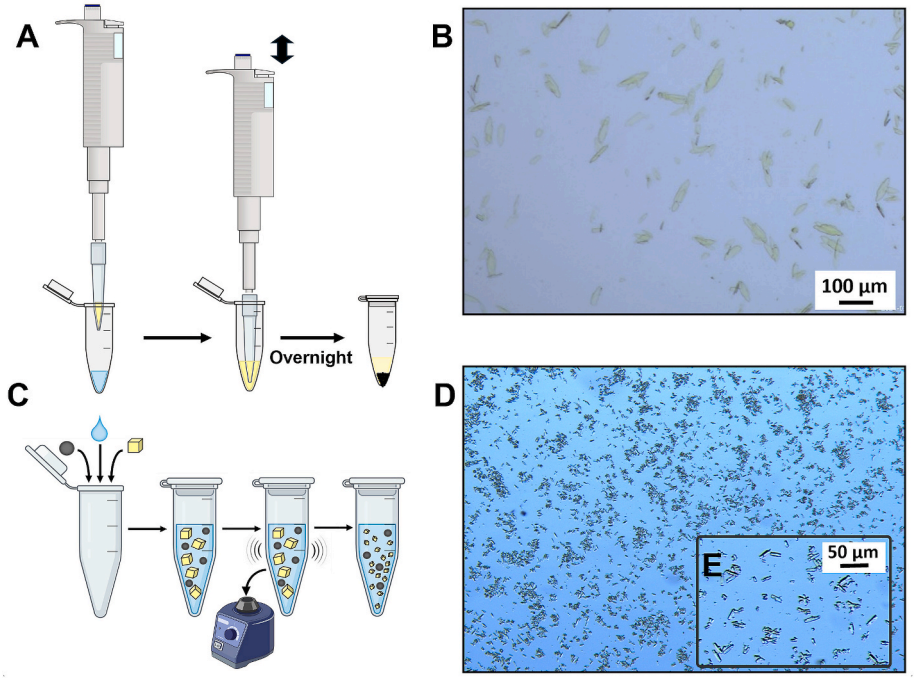

Fig. 1. Microcrystals of FPR obtained by the batch method. (A) Schematic of the batch method. A protein solution (22 mg/mL) was added dropwise to precipitant number 3 (as listed in Table S1) at a 1:2 ratio and mixed immediately using a micropipette for approximately 30 s. The mixture was then incubated overnight. **(B)** Large crystals of FPR_{ox} (100 μm) obtained as described in (A). **(C)** Schematic of seed production. FPR_{ox} seeds were produced by crushing the large FPR_{ox} crystals from (B) using glass beads and vortexing for 2 min. **(D)** FPR_{ox} microcrystals (25–35 μm) obtained using seeding. 1 μL of seeds from (C) was mixed with 100 μL of the same precipitant used in (A), then mixed as described in (A) with FPR_{ox} at 22 mg/mL in a 1:2 ratio. **(E)** Enlarged image of FPR_{ox} microcrystals.

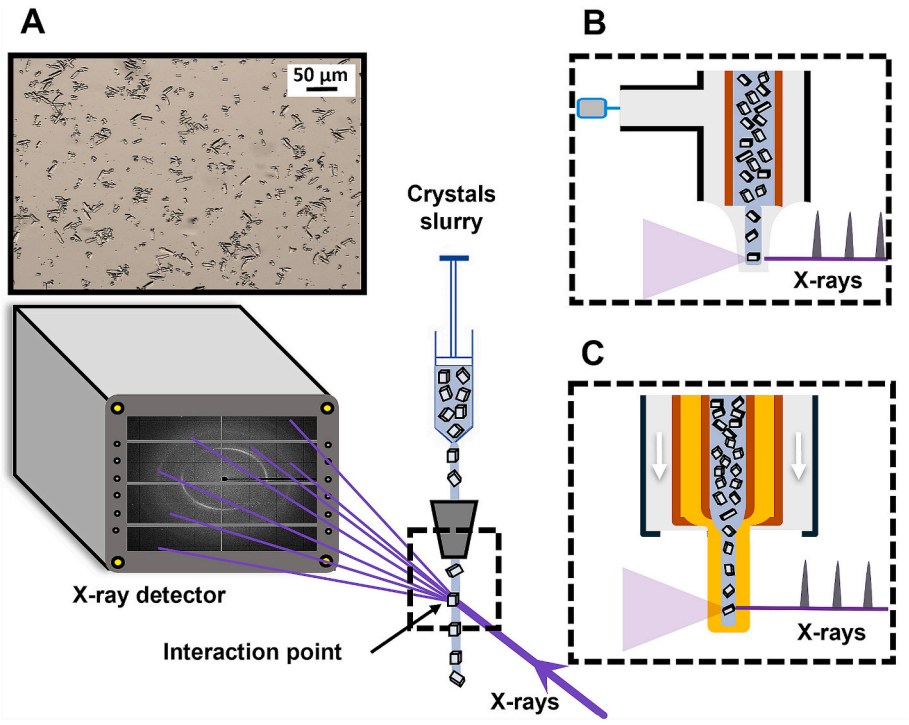

Fig. 2. Experimental setup of the SXF experiments carried out in this study. (A) FPR_{ox} microcrystals were delivered in a serial fashion, in random orientations, using **(B)** the MESH delivery device (helium gas sheath is shown in grey) and using the **(C)** delivery device DFFN (ethanol is shown in yellow and helium gas sheath is shown in grey) and they interact with the X-ray pulses at the interaction point.

XGANDALF [42], in that order. Intensities were integrated and merged into the point group *4* using CrystFEL's partialator.

In the case of EuXFEL data, a similar hit finding and indexing procedure was applied. Data was calibrated using Cheetah [38], and peakfinder8 was used to classify images as hits if they satisfied the following criteria: ADC threshold of 100, a minimum SNR of 7, and a minimum of one pixel per peak to identify at least 10 peaks across the detector. Indexing was attempted using the algorithms mosflm, xds [43,44].

The MTZ files for phasing and refinement were generated by the CTRUNCATE program [45] for LCLS data and SCALA program [46] for EuXFEL data from the CCP4 software package [47], with a fraction of 5 % reflections included in the generated R_{free} set. Initial phases were obtained by molecular replacement with PHASER [48] from PHENIX software suit [49] using the cryo-FPR_{ox} structure with PDB ID 6RR3 [23] as the search model. The obtained models were refined using alternate cycles of automated refinement with PHENIX.refine in the PHENIX software suite [49] and manual inspection performed with COOT [50]. The electron-density maps were calculated with the MAPS tool [49]. Structural figures presented in this study were generated with PyMol [51]. All data refinement statistics are listed in Table 1.

For structural comparison, B factors were also analyzed to assess the mobility of the C-terminal tail and the FAD relative to the rest of other protein atoms. To enable the comparison across different crystal structures, the B factors were normalized as previously reported [52,53], yielding a distribution with a mean of zero and a variance of one, according to the following formula:

$$Bnorm = \frac{B - < B >}{sd(B)}$$

where $< B >$ and sd(B) are the mean value and the standard deviation of the distribution of B factors for all protein atoms within each crystal structure, respectively. In this normalization, a B_{norm} value of 0 represents a water molecule with mobility equivalent to the average protein atom, while positive and negative values indicate higher or lower mobility, respectively, compared to the protein average.

2.6. Theoretical structural models for the Fdx:FPR and Fdx:FPR:$NADP^+$ complexes

The structural model for the binary Fdx:FPR interaction was constructed by using the AlphaFold 3 (AF3) server (https://alphafoldserver.com/) [54,55] and the corresponding protein sequences (Uniprot IDs A0A0H3ASL8 and A0A0H3ARI9 respectively for FPR and Fdx) from *B. ovis*. In addition to the protein folding, AF3 also incorporated the FAD cofactor into FPR, but not the [2Fe2S] cluster of Fdx. To introduce it, the model of the complex was superimposed to the crystal structure of Fd VI from *Rhodobacter Capsulatus* (PDB ID 1E9M), being the [2Fe2S] cluster directly transferred to the *B. ovis* Fdx:FPR AF3 model. The positioning of the $NADP^+$ coenzyme to produce the ternary Fdx:FPR:$NADP^+$ complex was carried out by structural comparison with the crystal structure of the cryo-FPR_{ox}:$NADP^+$ complex (PDB ID 6RRA). All models were analyzed using PyMol [51].

3. Results

3.1. FPR displays ferredoxin reductase activity

Fdx was overexpressed in *E. coli* Rosetta strain (DE3), being visible as a prominent band in an SDS-PAGE of extracted-cell lysates (Fig. S2). In these gels, the observed molecular weight of Fdx apparently varied along purification, and when pure appeared as at band of nearly (~20 kDa) twice of that theoretically calculated using ProtParam (11.5 kDa) (Fig. S2). This striking difference is usually found in [2Fe–2S] Fds exhibiting low isoelectric points (Fdx has a value of 4.02 according to ProtParam), which make them to establish unusual binding modes with SDS micelles decreasing their electrophoretic mobility [27]. A total of 6 mg of Fdx were obtained from 20 g of cells.

The purified Fdx was reddish-brown, as typically found in Fds containing the [2Fe–2S] cluster (Fig. 3A inset) [27], and showed an

Table 1
Data collection and refinement statistics for the room temperature structures of FPR from *B. ovis*. Values for the outer shell are given in parentheses.

	LCLS-FPR	EuXFEL-FPR
Data collection statistics		
X-ray source/beamline	LCLS/MFX	EuXFEL/SPB-SFX
Sample delivery	MESH	DFFN and C-type GDVN
Sample flow rate (μL/min)	3	20 (DFFN) and 40–50 (GDVN)
Photon energy (keV)	11.2	9.4
Wavelength (Å)	1.107 Å	1.319 Å
Repetition rate	120 Hz	1.1/0.5 MHz
Pulse duration (fs)	40	25
Beam size (μm) (FWHM)	3 × 4	1.6 × 1.6
Sample-to-detector distance (mm)	135	122
Temperature (K)	293 K	293 K
Detector	ePix10k	AGIPD 1MPx
Space group	$P4_1$	$P4_1$
a, b, c (Å)	a = 39.6 Å, b = 39.6 Å, c = 167.6 Å	a = 39.9 Å, b = 39.9 Å, c = 168.6 Å
α, β, γ (°)	α = β = γ = 90°	α = β = γ = 90°
Resolution range (Å)	35.2–2.1 (2.2–2.1)	23.0–1.9 (2.0–1.9)
No. of unique reflections	28 492 (2878)	20 670 (2013)
Completeness (%)	100 (100)	100 (100)
Multiplicity	413 (268)	48 (31)
Rsplit (%)	12.2 (170.4)	35.0 (106.9)
Avg. I/σ (I)	5.3 (0.2)	2.9 (0.8)
CC*	0.9949 (0.5825)	0.9479 (0.6284)
$CC_{1/2}$	0.9798 (0.2043)	0.8157 (0.2460)
Overall B factor from Wilson plot ($Å^2$)	76.24	24.2
Refinement Statistics		
Resolution range (Å)	35.8–2.2	22.97–1.90
No. of reflections, working set	13025	20610
No. of reflections, test set	5 %	5 %
R_{work}/R_{free} (%)	17.8/19.7	23.0/25.2
No. of non-H atoms		
Protein	2070	2070
Water	23	64
Others	53	53
R.m.s. deviations		
Bond length (Å)	0.002	0.002
Bond angles (°)	0.498	0.562
Ramachandran plot		
Favored (%)	1.57	1.18
Allowed (%)	98.43	98.82
Outliers (%)	0.0	0.0
PDB code	9GXC	9GXB

absorption spectrum with maxima at 340, 412, and 456 nm, as well as a noticeable shoulder at 510 nm (Fig. 3A). All these features are typical of [2Fe–2S] Fds [25,27]. The A_{340}/A_{280}, A_{412}/A_{280} and A_{456}/A_{280} ratios for pure Fdx showed values of 0.71, 0.56, and 0.47, respectively. Based on a ε_{458nm} (7.2 mM^{-1} cm^{-1}) for [2Fe2S] holo-Fdx a 1:1 cluster-to-peptide ratio, A_{456}/A_{280}, should be expected. Given the ratio A_{456}/A_{280} = 0.47, this agrees well with over 90 % of the here purified Fdx incorporating the [2Fe2S] redox cofactor [56,57].

When evaluating the produced Fdx as electron acceptor of FPR in the NADPH cytochrome *c* reductase assay, it was found that it was able to accept electrons from NADPH-reduced FPR and transfer them to the final cytochrome *c* acceptor. Controls in the absence of Fdx hardly showed NADPH cytochrome *c* reductase activity (which was subtracted from the one in the presence of Fdx), confirming that Fdx is required to mediate ET from FPR to cytochrome *c*. Under steady-state conditions, the rate constants for the process showed a Michaelis-Menten concentration profile (Fig. 3B), allowing to determine k_{cat} and K_M^{Fdx} values of 7.8 ± 0.4 s^{-1} and 4.2 ± 0.7 μM, respectively, at saturating concentrations of NADPH.

3.2. Room temperature structures of FPR_{ox} at XFELs

We have successfully determined the first room temperature structures of FPR_{ox} from *B. ovis* using data collected from serial femtosecond crystallography experiments at both the LCLS and the EuXFEL facilities. The crystals belonged to space group $P4_1$, with unit cell dimensions of a = 39.6 Å, b = 39.6 Å, c = 167.6, α = β = γ = 90° for LCLS, and a = 39.9 Å, b = 39.9 Å, c = 168.6 Å, α = β = γ = 90° for EuXFEL. FPR crystals diffracted to a resolution of 2.1 Å at the LCLS, while at the EuXFEL they reached 1.9 Å. Representative diffraction pattern of FPR microcrystals with diffraction up to 2.1 Å (LCLS) and 1.9 Å (EuXFEL) are shown in Fig. S3. At the LCLS, 1143469 frames were collected, with 306005 classified as hits and a percentage indexed, resulting in 80086 indexed, integrated, and merged lattices. The SLAC-FPR_{ox} structure was solved by molecular replacement using PDB ID 6RR3 [23] and refined to 2.2 Å resolution with R_{work} and R_{free} of 17.8 % and 19.7 %, respectively. At the EuXFEL, 1127566 frames were collected, with 3438 classified as hits and a percentage indexed, resulting in 3431 indexed, integrated, and merged lattices. The EuXFEL-FPR_{ox} structure was also solved by molecular replacement using PDB ID 6RR3 (Pérez-Amigot, Taleb et al., 2019) and refined to 1.9 Å resolution with R_{work} and R_{free} of 23.0 % and 25.2 %, respectively. The final structures at both facilities included one component in the asymmetric unit, as illustrated in Fig. 4. Full data collection and refinement statistics are provided in Table 1.

The two XFEL structures of FPR_{ox} were completely modeled from N-terminus to C-terminus, with uninterrupted residue sequences. The high quality of the structures is evident from the electron $2mF_o$-DF_c density maps around the FAD cofactor and the residues at the catalytic site (Fig. 4A). Both, like the previously reported cryo-FPR_{ox} and cryo-FPR_{ox}:$NADP^+$ structures, feature a six-stranded antiparallel β-barrel and a short α-helix in their N-terminal domains (residues 3–98) (Fig. 4B and **C**). Their C-terminal domains (residues 99–258) exhibit a Rossmann fold, typical of proteins that bind nucleotides. These structures also revealed some water molecules: 23 in the LCLS-FPR_{ox} structure and 64 in the EuXFEL-FPR_{ox} structure.

3.3. Structural comparison of room temperature FPR to related structures

Further evaluation of the quality of the two FPR_{ox} structures reported here was performed by comparing them with the crystal structure described for FPR under cryogenic conditions (PDB IDs 6RR3 and 6RRA [23]). Overall, our structures were in close alignment with the cryo-structures, with a root mean square deviation (R.M.S.D.) of 0.26/0.34 Å and 0.17/0.26 Å for the superposition of the C_α atoms of the cryo-FPR_{ox} structures (6RR3/6RRA) with the LCLS-FPR_{ox} and EuXFEL-FPR_{ox}-structures, respectively. Therefore, the overall folding of the FPR_{ox} protein chain and the FAD conformation are conserved among the available FPR_{ox} structures. Nevertheless, despite the similar folding of the protein chain, relevant differences are particularly observed in the degree of mobility of the cofactor FAD and the respective C-terminal tail regarding the rest of the structure. In the cryo-structures, the isoalloxazine and adenine rings of the cofactor exhibit the lower mobility values with respect to the protein average, being some of them close to the overall minimum (Fig. S4). In these structures, the FAD shows the higher mobility in the PPi and ribose moieties, especially in FPR_{ox} (6RR3). Moreover, in the cryo-FPR_{ox} structure the C-terminal tail appears more flexible than in the cryo-FPR_{ox}:$NADP^+$ structure, probably because the presence of $NADP^+$ (6RRA) limiting its mobility. In contrast, in our room temperature structures, the C-terminal has significantly higher B-factors than the protein average. In particular, B-factor values for the FAD PPi and ribose moieties in the EuXFEL-FPR_{ox} structure are close to the

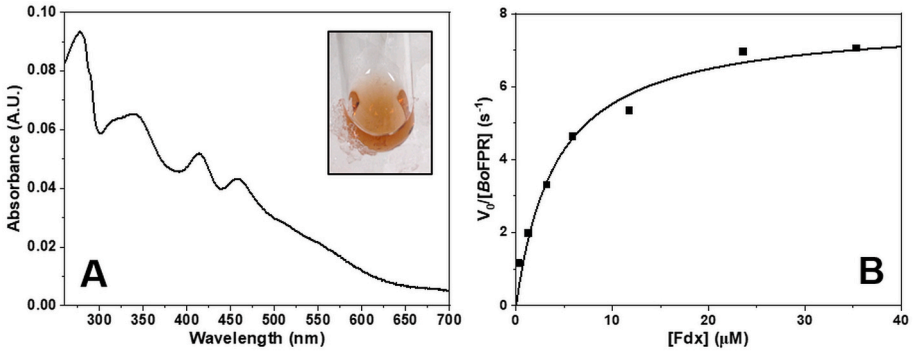

Fig. 3. Fdx as electron acceptor of FPR. (A) UV/visible absorption spectrum of Fdx_{ox} from *B. ovis* in 25 mM Tris/HCl, pH 7.2, 0.15 mM NaCl. The inset shows a picture of a pure Fdx fraction. **(B)** Michaelis-Menten plots for the NADPH-dependent cytochrome *c* reductase activity of FPR at 25 °C in 50 mM Tris/HCl pH 8.0 at saturating NADPH concentration (200 μM).

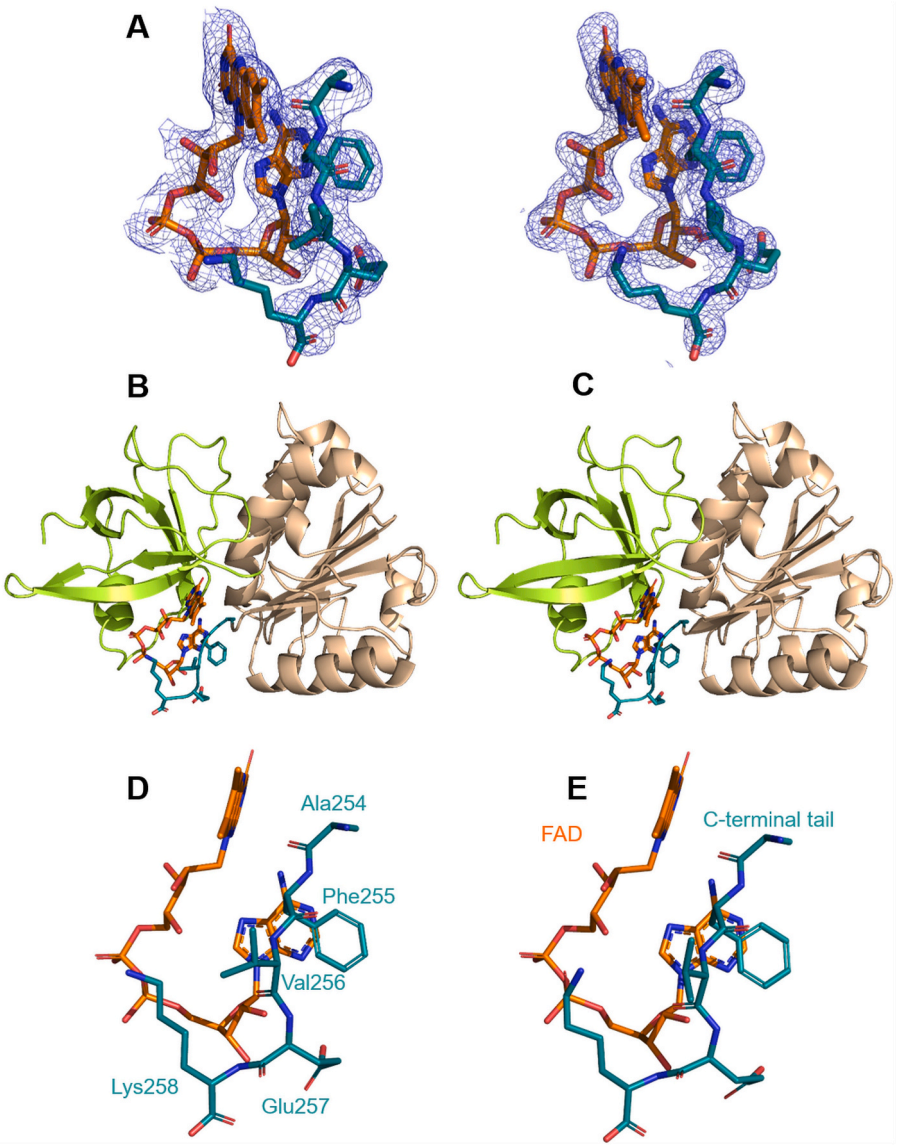

Fig. 4. Room temperature structures for *B. ovis* FPR_{ox}. (A) Electron density maps around the FAD cofactor and the C-terminal residues (254–258) of SLAC-FPR_{ox} (left) and EuXFEL-FPR_{ox} (right) structures, contoured at 0.6 and 0.9 sigma, respectively. Overall models for the **(B)** SLAC-FPR_{ox} and **(C)** EuXFEL-FPR_{ox} structures. The N-terminal domain, C-terminal domain and C-terminal tail are respectively shown in lime, wheat and deep teal. Detail at the active sites in the **(D)** SLAC-FPR_{ox} and **(E)** EuXFEL-FPR_{ox} structures of the spatial organization of the FAD and the C-terminal tail (254–258). In all panels the FAD cofactor is shown in CPK colored sticks with carbons in orange.

structure maximum (Fig. 5A). Noticeably, in this structure the FAD isoalloxazine and adenine rings also show the highest mobility among the rest of all compared structures. However, in the FPR_{ox}-LCLS structure, B-factors indicate a more flexible C-terminal (Fig. 5B). These features indicate overall higher FAD mobility in the room temperature structures, with its ribose and phosphate moieties being the most flexible parts.

The absence of the large loop interacting with the adenine moiety of FAD as observed in plastidic FNRs, together with the presence of a C-terminal tail absent in FNRs, causes the FAD cofactor to adopt a folded conformation in FPRs also in room temperature structures [17,58] (Figs. 4 and 5). As in the cryo-FPR_{ox} structures [23], Phe255 at the C-terminal tail stacks towards the adenine ring of the cofactor and the adenine ribose interacts with the C-terminal Val256 and Glu257 residues in both room temperature structures (Tables S2–S5). The C-terminal Lys258 residue interacts with the PPi in the FPR_{ox}-LCLS structure as in the cryo-FPR_{ox} and cryo-FPR_{ox}:$NADP^+$ structures, but such interaction is not observed in the EuXFEL-FPR_{ox} structure. The PPi moiety of our structures is also stabilized by residues Arg52, Leu77 and Thr78, similarly to both cryo-FPRs, and the polar interactions around the isoalloxazine ring are conserved. However, in the room temperature structures, the stabilizing contacts of the ribitol moiety of FAD with the protein chain are reduced to just one (Fig. 5 and Tables S2–S5), where the O3′ atom interacts with the O atom of Tyr54. This is partly due to the absence of interaction of O2' with Ala53, which is present in the cryo-structures, as well as to the fewer water molecules found in the room temperature structures. It is noteworthy that despite the low number of water molecules modeled in these later structures, one water molecule is consistently observed in all FPR_{ox} structures interacting with both the N5 atom of the isoalloxazine and the side chain of the catalytic Ser55 (which also H-bonds the N5 atom). In addition, the catalytic triad, Ser55, Cys220, and Glu252, typical of the FNR family and essential for interacting with the nicotinamide moiety of $NADP^+$/H for competent catalysis [18], maintains the same spatial orientation in the room temperature structures as observed in the cryo-FPR_{ox} structures.

Therefore, the room temperature structures of this study further suggest that during catalysis, the adenine of FAD, which is positioned between the isoalloxazine and nicotinamide reacting rings in the crystal structure, may become displaced. Moreover, B-factor values also suggest that the C-terminal tail might somehow contribute to that displacement in the case of FPRs.

3.4. The FPR structure can simultaneously allocate Fdx and $NADP^+$

It is well stablished that plastidic FNRs can simultaneously bind both the electron donor Fd and the $NADP^+$ hydride acceptor without displacing one another, with substrate binding being ordered to ensure efficient ET [3,59–62]. Nonetheless, these two binding sites have been shown not to be completely independent, as negative cooperativity has been observed in the ternary interaction when all components are in the oxidized state. Nonetheless, such negative cooperativity in binding appears translated into positive cooperativity at the kinetic level [3,4,60,61,63,64]. Given structural and functional similarities between plastidic FNRs and bacterial FPRs, the formation of a transient ternary complex could be also expected during the function of FPRs. Here, we have used AF3 to build a potential model for the binary interaction of Fdx and FPR

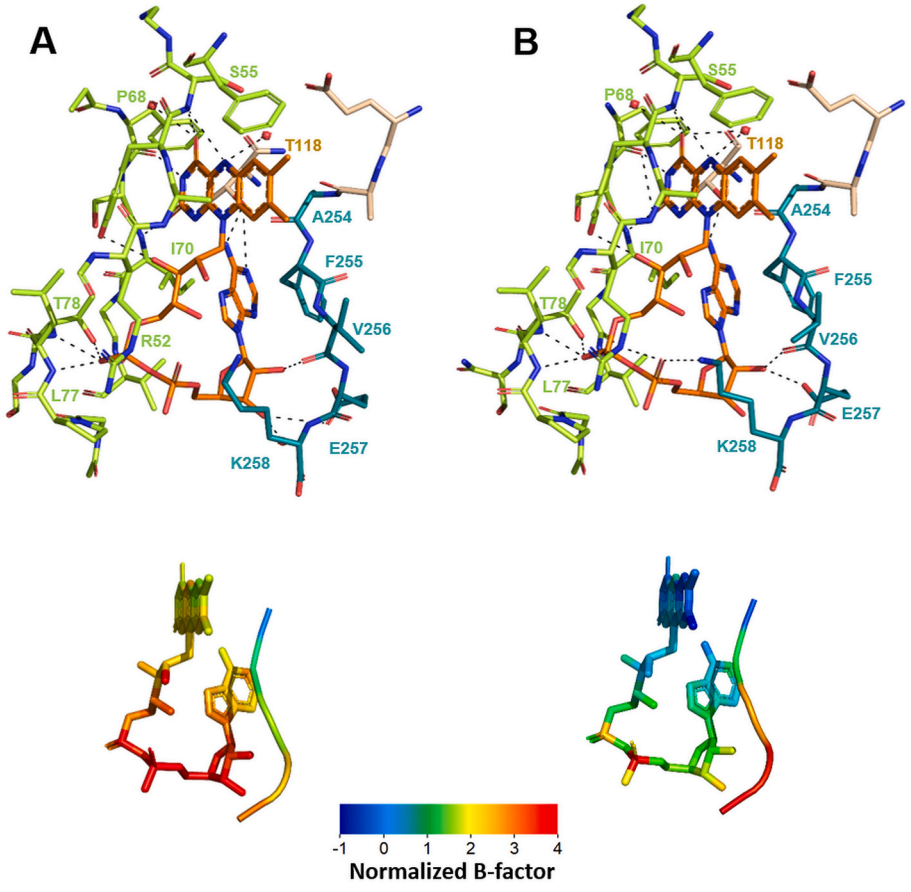

Fig. 5. FAD environment and normalized B-factors in the room temperature FPR structures. (A) SLAC-FPR_{ox} and **(B)** EuXFEL-FPR_{ox}. Top panels show the H-bond network stabilizing the FAD folded conformation in the FPR_{ox} structures. Polar contacts are represented by black dashed lines. These contacts and other interactions like carbon-pi, cation-pi and ring-ring are listened in Tables S4 and S5. Lower panels show normalized B-factors of FAD and C-terminal tail, as calculated by following the procedure indicated in section 2.5.

from *B. ovis* (Fig. S5). The top five models generated for the Fdx:FPR interaction were virtually identical, with predicted template modelling and interface predicted template modelling scores of 0.83 and 0.79, respectively; which is indicative of an overall high-confident prediction. When comparing this binary Fdx:FPR complex generated by AF3 with the cryo-FPR_{ox} (6RR3), SLAC-FPR_{ox} (9GXC), EuXFEL-FPR_{ox} (9GXB), and cryo-FPR_{ox}:$NADP^+$ (6RRA) structures, the RMSD values were 0.372 Å, 0.389 Å, 0.347 Å, and 0.343 Å, respectively. These low values suggest that the presence of Fdx does not induce significant structural changes in the reductase model. Based on our Fdx:FPR binary structural model, Fig. 6 illustrates the modeling of a putative Fdx:FNR:$NADP^+$ ternary complex by superimposing the AF3 binary model to the structure of the cryo-FPR_{ox}:$NADP^+$ complex (Fig. S1B). The resulting ternary complex reveals that the $NADP^+$ binding site on FPR does not overlap with the Fdx:FPR interface (Fig. 6), suggesting that the prior binding of either Fdx or $NADP^+$ to FPR should not interfere with the binding of the other substrate. However, due to the cryo-FPR_{ox}:$NADP^+$ template we used, the nicotinamide of the coenzyme is not optimally positioned for HT with the flavin isoalloxazine [23].

The molecular interface between Fdx and FPR in the model shows high complementarity characterized by a network of hydrophobic interactions (Fig. 6C). These interactions are mainly mediated by Met68, Met72 and Phe75 at the α-helix 68–75 of Fdx, which contact to Phe38, Met40 and the methyl groups of the FAD isoalloxazine. Additionally, the loop containing the residues 41 to 46 that houses the [2Fe2S] cluster in Fdx, also flanks the benzyl moiety of the flavin ring and stacks against the residues forming the characteristic C-terminal tail of FPRs. Moreover, the O of Ala46 in Fdx forms an H-bond with the N of Ala53 of FPR (a residue in the very close environment of the isoalloxazine ring), and two salt bridges are also present: $Asp74_{Fdx}$-$Lys95_{FPR}$ and $Glu40_{Fdx}$-$Arg52_{FPR}$. Thus, this model suggests that Fdx primarily binds to the N-terminal domain of FPR, with the [2Fe2S] cluster and the isoalloxazine ring being as close as 8.6 Å. Noticeably, the ternary model suggests that the C-terminal tail of FPR lies at the interface between the Fdx and $NADP^+$ binding sites on the reductase (Fig. 6). Specifically, it interacts with the Fdx loop containing the [2Fe2S] redox cluster, the PPi and adenine moieties of the FAD cofactor, and the NMN moiety of the $NADP^+$ coenzyme. Therefore, these observations suggest potential communication between the binding sites for both substrates and for the FAD cofactor through the arrangement of the C-terminal tail. Moreover, the presence of Fdx does not appear to introduce constrains within this ternary complex model that might prevent the adenine and/or C-terminus to shift to allow movement of the nicotinamide towards the flavin as suggested for the binary FNR:$NADP^+$/H complexes.

4. Discussion

Marked progress has been done in the past decades in understanding the structure-function relationships behind the kinetics of ET and HT processes involving FNRs and FPRs. However, many fundamental questions remain open regarding the function and regulation of FPR, as well as the molecular mechanism underlying such processes. In the case of the FPR from *B. ovis*, previous studies showed that it efficiently oxidizes NADPH, and its 2,6-Dichlorophenolindophenol diaphorase activity allowed determining k_{cat}, K_M^{NADPH}, and K_i values of $14.3 \pm 0.7\ s^{-1}$, 3.7 ± 0.2 μM, and 52 ± 8 μM, respectively [23]. Here, we show that the [2Fe2S] cluster of Fdx from *B. ovis* can accept electrons from the reduced NADPH FPR with a K_M^{Fdx} in the low μM range (Fig. 3B). This K_M^{Fdx} is in the range of those reported for the interaction of FPRs and FNRs with Fd/Fld electron carrier proteins [3–5,28,65,66]. This insight is valuable because it will aid in identifying the pathways through which electrons coming from FPR are utilized in the *B. ovis* metabolism. In pathogenic bacteria, Fd:FPR: systems have been reported to act as recycling redox systems, providing reducing power to mobilize the Fe^{3+} stored in the interior of Fe^{3+}-siderophore and bacterioferritin complexes and driving its reduction to Fe^{2+} [67,68]. In some bacteria, the biogenesis of iron-sulphur clusters, from a persulphide species (S^0) and Fe^{2+}, takes place through the IscS/IscU scaffold and the complex requires of an electron donor system [57,69–72]. In several species this is proposed to be a NADPH:FPR:Fd system. Two siderophores having key roles in virulence as well as the IscS/IscU system are present in *Brucella* species [73–75], suggesting these might be potential roles of the FPR:Fdx redox couple in *B. ovis*.

Iron is an essential element for all organisms and maintaining its balance is key for protecting against iron-induced toxicity, because free iron can promote the formation of ROS, such as superoxide, hydrogen peroxide, and hydroxyl radicals [76,77]. Therefore, free levels of iron must be tightly regulated to ensure metabolic needs while preventing toxicity. Some studies have shown that the FPR activity might contribute to ROS formation [78–81]. Others, indicate that the FPR action triggers the expression of the *soxRS* regulon that in turns protects cells against ROS [82], relying on a strict regulation of the NADPH/$NADP^+$ ratio to properly deploy such defensive response [82–84]. In this context, FPR is proposed to indirectly protect against ROS via NADPH oxidation without participation of Fd/Fld [79,82], but further research is necessary to elucidate the role played by FPRs in the regulation and prevention of mechanisms governing oxidative damage.

At the atomistic level it is well accepted that in both FNRs and FPRs, the HT process involving the $NADP^+$/H coenzyme occurs between the N5 atom of the FAD isoalloxazine and the C4 atom of the nicotinamide of $NADP^+$/H. In FNRs, the C-terminal tyrosine plays a crucial role in their high catalytic efficiency by: i) modulating the FAD midpoint reduction potential; ii) avoiding a too strong interaction between the reacting rings that would be incompatible with product release, iii) optimizing the geometry between the reacting atoms for HT; and iv) providing the active site with the required flexibility to allow the HT occurring through tunnel. In contrast, the folded conformation of FAD and the presence of the C-terminal tail in FPRs suggest a more complex mechanism for achieving the catalytically competent interaction [4,85]. In fact, during HT, active sites of FPRs have been reported to be in general more organized and rigid than those of FNRs [18]. These differences are likely due to the evolution of the active sites and catalytic mechanisms to fulfil their particular metabolic roles, establishing a compromise between protein flexibility and functional optimization.

The structural results of FPR_{ox} microcrystals produced at room temperature in this study highlight the adenine nucleotide moiety of FAD and the C-terminal tail of FPR_{ox} as the potentially flexible structural elements that may be displaced to form a coenzyme catalytic complex for HT (Fig. 5). In addition, the analysis of the crystal packing of the FPR_{ox} microcrystals (Fig. S6) reveals that the FAD cofactors are exposed within aqueous channels formed between monomers, allowing $NADP^+$/NADPH to approach and interact with FPR_{ox} at the active site. These preliminary findings suggest that FPR_{ox} microcrystals are suitable for mix-and-inject time-resolved studies at XFELs or synchrotrons (experiments currently underway), which could provide further insights into the dynamics and reaction mechanism of FPR with NADPH.

Here, we also predict that FPR can simultaneously bind both Fdx and $NADP^+$ (Fig. 6). This observation could be related to the potential regulation of the overall HT/ET processes from NADPH to Fdx, similar to what has been proposed for plastidic FNRs [3,4,59,61,63,86]. Consequently, potential structural rearrangements in the regions making the Fdx:FPR binary interaction may depend on the redox states of their [2Fe2S] and FAD cofactors. Thus, the Fdx's redox state might influence the conformation of the loop holding its [2Fe2S] cluster, which in turn could affect the conformation of the adjacent C-terminal tail of FPR. Changes in the redox state of Fdx might trigger subsequent conformational changes in the C-terminal tail, potentially impacting the FAD conformation and thereby altering the affinity and orientation of $NADP^+$/H. Similarly, variations in the redox state of the coenzyme or of the cofactor could alter the FPR's affinity for Fdx and contribute to its release upon ET. In fact, in the case of plastidic Fd, displacement of the loop holding the redox cluster upon change in redox state has been

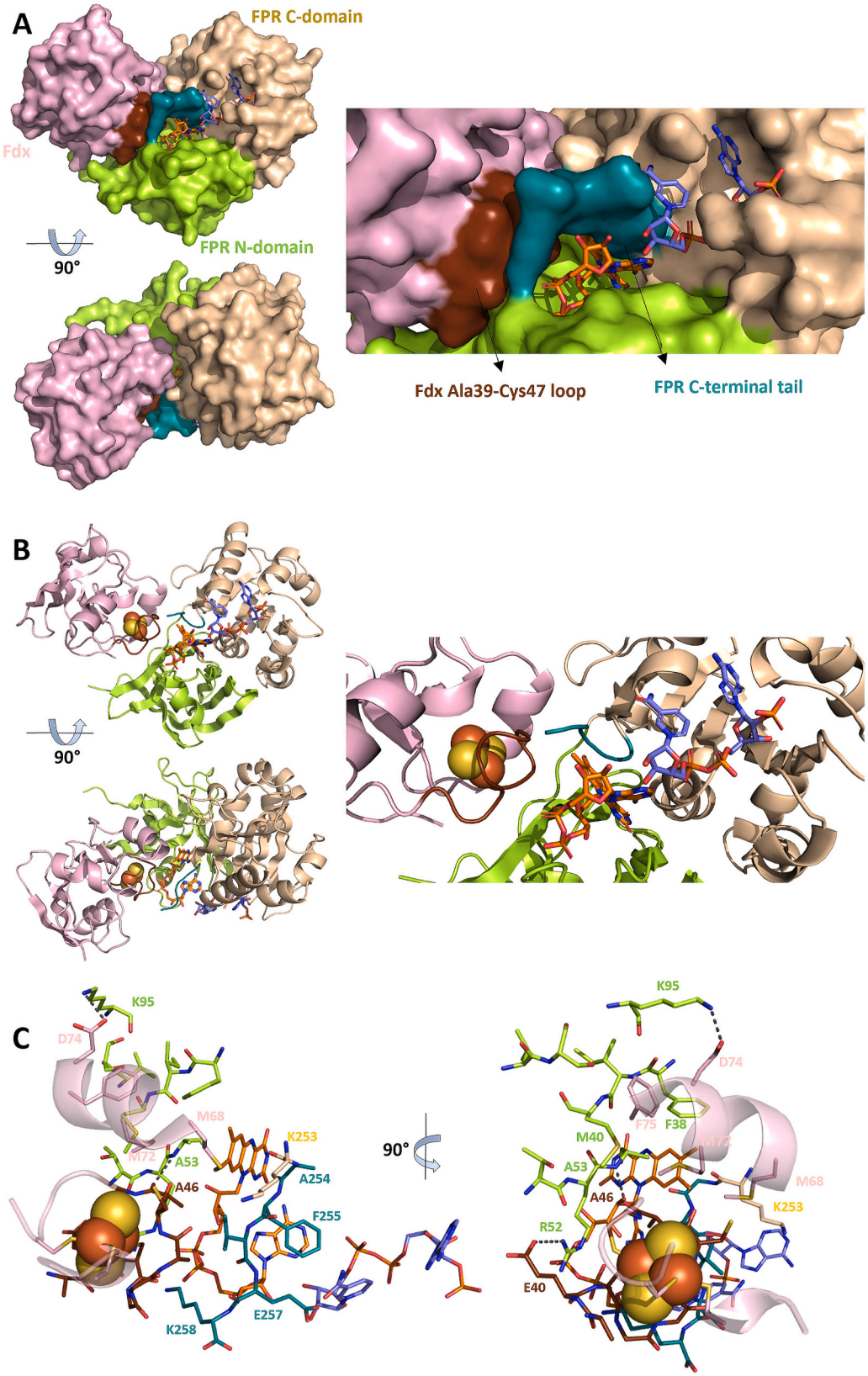

Fig. 6. Model of a Fdx:FPR:NADP + ternary complex in *B. ovis*. Overall view of the ternary complex model as **(A)** surface and **(B)** cartoon. Right panels show a zoom at the interface of the three components. **(C)** Detail of the arrangement of redox centers and the residues involved in the Fdx:FPR binary interaction. Fdx is shown in light pink with the Ala39-Cys47-loop in chocolate, while for FPR the N-terminal domain, C-terminal domain and C-terminal tail are respectively shown in lime, wheat and teal. The FAD cofactor and the $NADP^+$ coenzyme are shown in sticks with carbons respectively in orange and violet, while the [2Fe2S] cluster of Fdx is shown in CPK colored spheres. Superposition of the coordinates of the binary modeled complex with those of the cryo-FPR_{ox}:$NADP^+$ complex from *B. ovis* (6RAA) and Fd VI from *Rhodobacter Capsulatus* (PDB 1E9M) allowed to place the $NADP^+$ coenzyme on to the FPR chain and the [2Fe2S] on the Fdx one.

associated with the different affinity of FNR for oxidized and reduced Fd, and it is thought to play a role in the release of oxidized Fd after ET to FNR takes place [61,87–90].

The study presented here, shows that FPR can use Fdx as electron acceptor. This finding opens new avenues for exploring FPR's relevance in the *B. ovis* physiology. In addition, this study provides new tools for examining at the atomic and molecular level conformational changes in FPR during the HT process from NADPH. We also provide with a potential model for a ternary Fdx:FPR:NADPH complex that could contribute to modulate the HT and ET processes involved in FPR activity. This research lays the groundwork for future studies to clarify the functions and molecular features of FPRs in general, and particularly those of FPR from *B. ovis*. FPR conformational dynamics during catalysis remains unexplained because the expected molecular movements for the nicotinamide stacking against the isoalloxazine of the FAD are not evident. Future research is required to identify the main molecular intermediates and final species of the equilibrium mixture in the ET and HT processes within competent binary and ternary complexes, and to understand the role of coupled proton transfer coupled in efficiency of ET from FPR_{rd} to oxidized Fdx. We have yet to uncover how the presence of Fdx might modulate the HT from NADPH to FPR_{ox}, or how the presence of the coenzyme modulates the interaction and ET between FPR and Fdx at the atomistic, molecular, and dynamic levels. As these reactions are essential to bacterial survival, resolving these questions will aid in exploring FPRs as potential antimicrobial targets.

CRediT authorship contribution statement

Andrea Moreno: Writing – original draft, Methodology, Investigation. **Isabel Quereda-Moraleda:** Writing – original draft, Methodology, Investigation. **Celia Lozano-Vallhonrat:** Investigation. **María Buñuel-Escudero:** Investigation. **Sabine Botha:** Writing – original draft, Methodology, Investigation. **Christopher Kupitz:** Resources, Methodology, Investigation. **Stella Lisova:** Resources. **Ray Sierra:** Software, Resources, Methodology. **Valerio Mariani:** Software, Resources, Methodology. **Pamela Schleissner:** Resources, Methodology. **Leland B. Gee:** Software, Resources, Methodology. **Katerina Dörner:** Resources, Methodology. **Christina Schmidt:** Resources, Methodology. **Huijong Han:** Resources, Methodology. **Marco Kloos:** Resources, Methodology. **Peter Smyth:** Resources, Methodology. **Joana Valerio:** Resources, Methodology. **Joachim Schulz:** Resources, Methodology. **Raphael de Wijn:** Writing – review & editing, Software, Resources, Methodology. **Diogo V.M. Melo:** Software, Resources, Methodology. **Adam Round:** Software, Resources, Methodology. **Fabian Trost:** Resources. **Egor Sobolev:** Resources. **E. Juncheng:** Resources. **Marcin Sikorski:** Resources. **Richard Bean:** Writing – review & editing, Software, Resources, Methodology. **Marta Martínez-Júlvez:** Writing – review & editing, Writing – original draft, Visualization, Validation, Supervision, Investigation, Formal analysis, Data curation. **Jose Manuel Martin-Garcia:** Writing – review & editing, Writing – original draft, Visualization, Validation, Supervision, Project administration, Methodology, Investigation, Funding acquisition, Formal analysis, Data curation, Conceptualization. **Milagros Medina:** Writing – review & editing, Writing – original draft, Visualization, Validation, Supervision, Project administration, Methodology, Investigation, Funding acquisition, Formal analysis, Data curation, Conceptualization.

Data availability

The structural data for the generated FPR structures in this study are available in the Protein Data Bank repository (https://www.rcsb.org/) under accession PDB codes 9GXB and 9GXC.

Conflicts of interests statement

The authors declare no competing interests.

Acknowledgements

This work has been funded by the Spanish State Research Agency and by FEDER (MCIN/AEI-FEDER, Grant PID2022-136369NB-I00) and the Government of Aragón-FEDER (Grants LMP13_21 and E35_23R). MCIN/AEI/10.13039/501100011033/ERDF (Grant MCIN/AEI/PID2022-136369NBI00); Ayuda de Atracción y Retención de Talento Investigador from the Community of Madrid (Grants 2019-T1/BMD-15552, 2023-5A/BMD-28921). The European Union NextGenerationEU/PRTR (Grant number CNS2022-135713). XFEL experiments were performed at MFX beamline at the LCLS and SPB/SFX at the EuXFEL during proposals P10027 and P5458, respectively. Authors would like to acknowledge Servicios Generales de Apoyo a la Investigación-SAI, Universidad de Zaragoza, for its support.

Appendix A. Supplementary data

Supplementary data to this article can be found online at https://doi.org/10.1016/j.abb.2024.110204.

References

[1] E.A. Ceccarelli, A.K. Arakaki, N. Cortez, N. Carrillo, Functional plasticity and catalytic efficiency in plant and bacterial ferredoxin-NADP(H) reductases, Biochim. Biophys. Acta 1698 (2) (2004) 155–165.
[2] A. Aliverti, V. Pandini, A. Pennati, M. de Rosa, G. Zanetti, Structural and functional diversity of ferredoxin-NADP+ reductases, Arch. Biochem. Biophys. 474 (2) (2008) 283–291.
[3] M. Medina, Structural and mechanistic aspects of flavoproteins: photosynthetic electron transfer from photosystem I to NADP+, FEBS J. 276 (15) (2009) 3942–3958.
[4] P. Mulo, M. Medina, Interaction and electron transfer between ferredoxin-NADP$^+$ oxidoreductase and its partners: structural, functional, and physiological implications, Photosynth. Res. 134 (3) (2017) 265–280.
[5] A. Palavecino, M.G. Sartorio, N. Carrillo, N. Cortez, A. Bortolotti, The extremophilic Andean isolate Acinetobacter sp. Ver3 expresses two ferredoxin-NADP, FEBS Lett. 598 (6) (2024) 670–683.
[6] I. Nogués, I. Pérez-Dorado, S. Frago, C. Bittel, S.G. Mayhew, C. Gómez-Moreno, J. A. Hermoso, M. Medina, N. Cortez, N. Carrillo, The ferredoxin-NADP(H) reductase from Rhodobacter capsulatus: molecular structure and catalytic mechanism, Biochemistry 44 (35) (2005) 11730–11740.
[7] C. Bittel, L.C. Tabares, M. Armesto, N. Carrillo, N. Cortez, The oxidant-responsive diaphorase of Rhodobacter capsulatus is a ferredoxin (flavodoxin)-NADP(H) reductase, FEBS Lett. 553 (3) (2003) 408–412.
[8] I. Nogues, M. Hervas, J. Peregrina, J. Navarro, M. de la Rosa, C. Gomez-Moreno, M. Medina, Anabaena flavodoxin as an electron carrier from photosystem I to ferredoxin-NADP(+) reductase. Role of flavodoxin residues in protein-protein interaction and electron transfer, Biochemistry 44 (1) (2005) 97–104.
[9] M. Giro, N. Carrillo, A.R. Krapp, Glucose-6-phosphate dehydrogenase and ferredoxin-NADP(H) reductase contribute to damage repair during the soxRS response of Escherichia coli, Microbiology 152 (Pt 4) (2006) 1119–1128.
[10] A. Bortolotti, I. Pérez-Dorado, G. Goñi, M. Medina, J.A. Hermoso, N. Carrillo, N. Cortez, Coenzyme binding and hydride transfer in Rhodobacter capsulatus ferredoxin/flavodoxin NADP(H) oxidoreductase, Biochim. Biophys. Acta 1794 (2) (2009) 199–210.
[11] M. Sanchez-Azqueta, B. Herguedas, R. Hurtado-Guerrero, M. Hervas, J.A. Navarro, M. Martinez-Julvez, M. Medina, A hydrogen bond network in the active site of Anabaena ferredoxin-NADP(+) reductase modulates its catalytic efficiency, Biochim. Biophys. Acta Bioenerg. 1837 (2) (2014) 251–263.
[12] E.G. Orellano, N.B. Calcaterra, N. Carrillo, E.A. Ceccarelli, Probing the role of the carboxyl-terminal region of ferredoxin-NADP+ reductase by site-directed mutagenesis and deletion analysis, J. Biol. Chem. 268 (26) (1993) 19267–19273.
[13] L. Piubelli, A. Aliverti, A.K. Arakaki, N. Carrillo, E.A. Ceccarelli, P.A. Karplus, G. Zanetti, Competition between C-terminal tyrosine and nicotinamide modulates pyridine nucleotide affinity and specificity in plant ferredoxin-NADP+ reductase, J. Biol. Chem. 275 (14) (2000) 10472–10476.
[14] I. Nogués, J. Tejero, J.K. Hurley, D. Paladini, S. Frago, G. Tollin, S.G. Mayhew, C. Gómez-Moreno, E.A. Ceccarelli, N. Carrillo, M. Medina, Role of the C-terminal tyrosine of ferredoxin-nicotinamide adenine dinucleotide phosphate reductase in the electron transfer processes with its protein partners ferredoxin and flavodoxin, Biochemistry 43 (20) (2004) 6127–6137.
[15] I. Pérez-Dorado, A. Bortolotti, N. Cortez, J.A. Hermoso, Crystallization of a flavodoxin involved in nitrogen fixation in Rhodobacter capsulatus, Acta Crystallogr., Sect. F: Struct. Biol. Cryst. Commun. 64 (Pt 5) (2008) 375–377.
[16] M.L. Tondo, M.A. Musumeci, M.L. Delprato, E.A. Ceccarelli, E.G. Orellano, Structural-functional characterization and physiological significance of ferredoxin-NADP+ reductase from Xanthomonas axonopodis pv, citri, PLoS One 6 (11) (2011) e27124.

[17] A. Bortolotti, A. Sánchez-Azqueta, C.M. Maya, A. Velázquez-Campoy, J. A. Hermoso, M. Medina, N. Cortez, The C-terminal extension of bacterial flavodoxin-reductases: involvement in the hydride transfer mechanism from the coenzyme, Biochim. Biophys. Acta 1837 (1) (2014) 33–43.

[18] A. Sánchez-Azqueta, D.L. Catalano-Dupuy, A. López-Rivero, M.L. Tondo, E. G. Orellano, E.A. Ceccarelli, M. Medina, Dynamics of the active site architecture in plant-type ferredoxin-NADP(+) reductases catalytic complexes, Biochim. Biophys. Acta 1837 (10) (2014) 1730–1738.

[19] G. Sridhar Prasad, N. Kresge, A.B. Muhlberg, A. Shaw, Y.S. Jung, B.K. Burgess, C. D. Stout, The crystal structure of NADPH:ferredoxin reductase from Azotobacter vinelandii, Protein Sci. 7 (12) (1998) 2541–2549.

[20] A. Wang, Y. Zeng, H. Han, S. Weeratunga, B.N. Morgan, P. Moenne-Loccoz, E. Schonbrunn, M. Rivera, Biochemical and structural characterization of Pseudomonas aeruginosa Bfd and FPR: ferredoxin NADP+ reductase and not ferredoxin is the redox partner of heme oxygenase under iron-starvation conditions, Biochemistry 46 (43) (2007) 12198–12211.

[21] M.L. Tondo, R. Hurtado-Guerrero, E.A. Ceccarelli, M. Medina, E.G. Orellano, M. Martinez-Julvez, Crystal structure of the FAD-containing ferredoxin-NADP (+) reductase from the plant pathogen xanthomonas axonopodis pv. citri, BioMed Res. Int. 2013 (2013) ID906572.

[22] M. Minjárez-Sáenz, M. Martínez-Júlvez, I. Yruela, M. Medina, Mining the flavoproteome of Brucella ovis, the brucellosis causing agent in Ovis aries, Microbiol. Spectr. 10 (2) (2022) e0229421.

[23] D. Pérez-Amigot, V. Taleb, S. Boneta, E. Anoz-Carbonell, M. Sebastián, A. Velázquez-Campoy, V. Polo, M. Martínez-Júlvez, M. Medina, Towards the competent conformation for catalysis in the ferredoxin-NADP+ reductase from the Brucella ovis pathogen, Biochim. Biophys. Acta Bioenerg. 1860 (10) (2019) 148058.

[24] A. Wang, J.C. Rodríguez, H. Han, E. Schönbrunn, M. Rivera, X-ray crystallographic and solution state nuclear magnetic resonance spectroscopic investigations of NADP+ binding to ferredoxin NADP reductase from Pseudomonas aeruginosa, Biochemistry 47 (31) (2008) 8080–8093.

[25] S. Adinolfi, F. Rizzo, L. Masino, M. Nair, S.R. Martin, A. Pastore, P.A. Temussi, Bacterial IscU is a well folded and functional single domain protein, Eur. J. Biochem. 271 (11) (2004) 2093–2100.

[26] J.J. Pueyo, C. Gómez-Moreno, Purification of ferredoxin-NADP+ reductase, flavodoxin and ferredoxin from a single batch of the cyanobacterium Anabaena PCC 7119, Prep. Biochem. 21 (4) (1991) 191–204.

[27] H. Huang, L. Hu, W. Yu, H. Li, F. Tao, H. Xie, S. Wang, Heterologous overproduction of 2[4Fe4S]- and [2Fe2S]-type clostridial ferredoxins and [2Fe2S]-type agrobacterial ferredoxin, Protein Expr. Purif. 121 (2016) 1–8.

[28] M. Medina, M. Martinez-Julvez, J.K. Hurley, G. Tollin, C. Gomez-Moreno, Involvement of glutamic acid 301 in the catalytic mechanism of ferredoxin-NADP(+) reductase from Anabaena PCC 7119, Biochemistry 37 (9) (1998) 2715–2728.

[29] C.M. Jenkins, C.G. Genzor, M.F. Fillat, M.R. Waterman, C. Gómez-Moreno, Negatively charged Anabaena flavodoxin residues (Asp144 and Glu145) are important for reconstitution of cytochrome P450 17alpha-hydroxylase activity, J. Biol. Chem. 272 (36) (1997) 22509–22513.

[30] C. Kupitz, I. Grotjohann, C.E. Conrad, S. Roy-Chowdhury, R. Fromme, P. Fromme, Microcrystallization techniques for serial femtosecond crystallography using photosystem II from Thermosynechococcus elongatus as a model system, Philos. Trans. R. Soc. Lond. B Biol. Sci. 369 (1647) (2014) 20130316.

[31] R.G. Sierra, A. Batyuk, Z. Sun, A. Aquila, M.S. Hunter, T.J. Lane, M. Liang, C. H. Yoon, R. Alonso-Mori, R. Armenta, J.C. Castagna, M. Hollenbeck, T.O. Osier, M. Hayes, J. Aldrich, R. Curtis, J.E. Koglin, T. Rendahl, E. Rodriguez, S. Carbajo, S. Guillet, R. Paul, P. Hart, K. Nakahara, G. Carini, H. DeMirci, E.H. Dao, B. M. Hayes, Y.P. Rao, M. Chollet, Y. Feng, F.D. Fuller, C. Kupitz, T. Sato, M. H. Seaberg, S. Song, T.B. van Driel, H. Yavas, D. Zhu, A.E. Cohen, S. Wakatsuki, S. Boutet, The macromolecular femtosecond crystallography instrument at the linac coherent light source, J. Synchrotron Radiat. 26 (Pt 2) (2019) 346–357.

[32] R.G. Sierra, C. Gati, H. Laksmono, E.H. Dao, S. Gul, F. Fuller, J. Kern, R. Chatterjee, M. Ibrahim, A.S. Brewster, I.D. Young, T. Michels-Clark, A. Aquila, M. Liang, M. S. Hunter, J.E. Koglin, S. Boutet, E.A. Junco, B. Hayes, M.J. Bogan, C.Y. Hampton, E.V. Puglisi, N.K. Sauter, C.A. Stan, A. Zouni, J. Yano, V.K. Yachandra, S.M. Soltis, J.D. Puglisi, H. DeMirci, Concentric-flow electrokinetic injector enables serial crystallography of ribosome and photosystem II, Nat. Methods 13 (1) (2016) 59–62.

[33] T.B. van Driel, S. Nelson, R. Armenta, G. Blaj, S. Boo, S. Boutet, D. Doering, A. Dragone, P. Hart, G. Haller, C. Kenney, M. Kwaitowski, L. Manger, M. McKelvey, K. Nakahara, M. Oriunno, T. Sato, M. Weaver, The ePix10k 2-megapixel hard X-ray detector at LCLS, J. Synchrotron Radiat. 27 (Pt 3) (2020) 608–615.

[34] V. Mariani, A. Morgan, C.H. Yoon, T.J. Lane, T.A. White, C. O'Grady, M. Kuhn, S. Aplin, J. Koglin, A. Barty, H.N. Chapman, Online data analysis and feedback for serial X-ray imaging, J. Appl. Crystallogr. 49 (Pt 3) (2016) 1073–1080.

[35] D. Oberthuer, J. Knoška, M.O. Wiedorn, K.R. Beyerlein, D.A. Bushnell, E. G. Kovaleva, M. Heymann, L. Gumprecht, R.A. Kirian, A. Barty, V. Mariani, A. Tolstikova, L. Adriano, S. Awel, M. Barthelmess, K. Dörner, P.L. Xavier, O. Yefanov, D.R. James, G. Nelson, D. Wang, G. Calvey, Y. Chen, A. Schmidt, M. Szczepek, S. Frielingsdorf, O. Lenz, E. Snell, P.J. Robinson, B. Šarler, G. Belšak, M. Maček, F. Wilde, A. Aquila, S. Boutet, M. Liang, M.S. Hunter, P. Scheerer, J. D. Lipscomb, U. Weierstall, R.D. Kornberg, J.C. Spence, L. Pollack, H.N. Chapman, S. Bajt, Double-flow focused liquid injector for efficient serial femtosecond crystallography, Sci. Rep. 7 (2017) 44628.

[36] M. Vakili, J. Bielecki, J. Knoška, F. Otte, H. Han, M. Kloos, R. Schubert, E. Delmas, G. Mills, R. de Wijn, R. Letrun, S. Dold, R. Bean, A. Round, Y. Kim, F.A. Lima, K. Dörner, J. Valerio, M. Heymann, A.P. Mancuso, J. Schulz, 3D printed devices and infrastructure for liquid sample delivery at the European XFEL, J. Synchrotron Radiat. 29 (Pt 2) (2022) 331–346.

[37] A. Allahgholi, J. Becker, A. Delfs, R. Dinapoli, P. Goettlicher, D. Greiffenberg, B. Henrich, H. Hirsemann, M. Kuhn, R. Klanner, A. Klyuev, H. Krueger, S. Lange, T. Laurus, A. Marras, D. Mezza, A. Mozzanica, M. Niemann, J. Poehlsen, J. Schwandt, I. Sheviakov, X. Shi, S. Smoljanin, L. Steffen, J. Sztuk-Dambietz, U. Trunk, Q. Xia, M. Zeribi, J. Zhang, M. Zimmer, B. Schmitt, H. Graafsma, The adaptive gain integrating pixel detector at the European XFEL, J. Synchrotron Radiat. 26 (Pt 1) (2019) 74–82.

[38] A. Barty, R.A. Kirian, F.R. Maia, M. Hantke, C.H. Yoon, T.A. White, H. Chapman, Software for high-throughput reduction and analysis of serial femtosecond X-ray diffraction data, J. Appl. Crystallogr. 47 (Pt 3) (2014) 1118–1131.

[39] T.A. White, R.A. Kirian, A.V. Martin, A. Aquila, K. Nass, A. Barty, H.N. Chapman, CrystFEL: a software suite for snapshot serial crystallography, Journal of Applied Crystallography %@ 0021-8898 45 (2) (2012) 335–341.

[40] T.A. White, Processing serial crystallography data with CrystFEL: a step-by-step guide, Acta Crystallogr D Struct Biol 75 (Pt 2) (2019) 219–233.

[41] T.G. Battye, L. Kontogiannis, O. Johnson, H.R. Powell, A.G. Leslie, iMOSFLM: a new graphical interface for diffraction-image processing with MOSFLM, Acta Crystallogr D Biol Crystallogr 67 (Pt 4) (2011) 271–281.

[42] Y. Gevorkov, O. Yefanov, A. Barty, T.A. White, V. Mariani, W. Brehm, A. Tolstikova, R.R. Grigat, H.N. Chapman, Xgandalf - extended gradient descent algorithm for lattice finding, Acta Crystallogr A Found Adv 75 (Pt 5) (2019) 694–704.

[43] W. Kabsch, Xds, Acta Crystallogr D Biol Crystallogr 66 (Pt 2) (2010) 125–132.

[44] A. Duisenberg, Indexing in single-crystal diffractometry with an obstinate list of reflections, Journal of Applied Crystallography %@ 0021-8898 25 (2) (1992) 92–96.

[45] P.R. Evans, An introduction to data reduction: space-group determination, scaling and intensity statistics, Acta Crystallogr D Biol Crystallogr 67 (Pt 4) (2011) 282–292.

[46] P. Evans, Scaling and assessment of data quality, Acta Crystallogr D Biol Crystallogr 62 (Pt 1) (2006) 72–82.

[47] M.D. Winn, C.C. Ballard, K.D. Cowtan, E.J. Dodson, P. Emsley, P.R. Evans, R. M. Keegan, E.B. Krissinel, A.G. Leslie, A. McCoy, S.J. McNicholas, G.N. Murshudov, N.S. Pannu, E.A. Potterton, H.R. Powell, R.J. Read, A. Vagin, K.S. Wilson, Overview of the CCP4 suite and current developments, Acta Crystallogr D Biol Crystallogr 67 (Pt 4) (2011) 235–242.

[48] A.J. McCoy, R.W. Grosse-Kunstleve, P.D. Adams, M.D. Winn, L.C. Storoni, R. J. Read, Phaser crystallographic software, J. Appl. Crystallogr. 40 (Pt 4) (2007) 658–674.

[49] D. Liebschner, P.V. Afonine, M.L. Baker, G. Bunkóczi, V.B. Chen, T.I. Croll, B. Hintze, L.W. Hung, S. Jain, A.J. McCoy, N.W. Moriarty, R.D. Oeffner, B.K. Poon, M.G. Prisant, R.J. Read, J.S. Richardson, D.C. Richardson, M.D. Sammito, O. V. Sobolev, D.H. Stockwell, T.C. Terwilliger, A.G. Urzhumtsev, L.L. Videau, C. J. Williams, P.D. Adams, Macromolecular structure determination using X-rays, neutrons and electrons: recent developments in Phenix, Acta Crystallogr D Struct Biol 75 (Pt 10) (2019) 861–877.

[50] P. Emsley, B. Lohkamp, W.G. Scott, K. Cowtan, Features and development of coot, Acta Crystallogr D Biol Crystallogr 66 (Pt 4) (2010) 486–501.

[51] W.L. Delano, PyMOL: an open-source molecular graphics tool, CCP4 Newsletter On Protein Crystallography 40 (2002) 82–92.

[52] Y. Lu, R. Wang, C.Y. Yang, S. Wang, Analysis of ligand-bound water molecules in high-resolution crystal structures of protein-ligand complexes, J. Chem. Inf. Model. 47 (2) (2007) 668–675.

[53] J.M. Martin-Garcia, J. Ruiz-Sanz, I. Luque, Interfacial water molecules in SH3 interactions: a revised paradigm for polyproline recognition, Biochem. J. 442 (2) (2012) 443–451.

[54] R. Evans, M. O'Neill, A. Pritzel, N. Antropova, A. Senior, T. Green, A. Žídek, R. Bates, S. Blackwell, J. Yim, O. Ronneberger, S. Bodenstein, M. Zielinski, A. Bridgland, A. Potapenko, A. Cowie, K. Tunyasuvunakool, R. Jain, E. Clancy, P. Kohli, J. Jumper, D. Hassabis, Protein complex prediction with AlphaFold-Multimer, bioRxiv (2022), 2021.10.04.463034.

[55] M. Mirdita, K. Schütze, Y. Moriwaki, L. Heo, S. Ovchinnikov, M. Steinegger, ColabFold: making protein folding accessible to all, Nat. Methods 19 (6) (2022) 679–682.

[56] Y.S. Jung, V.A. Roberts, C.D. Stout, B.K. Burgess, Complex formation between Azotobacter vinelandii ferredoxin I and its physiological electron donor NADPH-ferredoxin reductase, J. Biol. Chem. 274 (5) (1999) 2978–2987.

[57] R. Yan, S. Adinolfi, C. Iannuzzi, G. Kelly, A. Oregioni, S. Martin, A. Pastore, Cluster and fold stability of E. coli ISC-type ferredoxin, PLoS One 8 (11) (2013) e78948.

[58] L. Serre, F.M. Vellieux, M. Medina, C. Gómez-Moreno, J.C. Fontecilla-Camps, M. Frey, X-ray structure of the ferredoxin:NADP+ reductase from the cyanobacterium Anabaena PCC 7119 at 1.8 Å resolution, and crystallographic studies of NADP+ binding at 2.25 Å resolution, J. Mol. Biol. 263 (1) (1996) 20–39.

[59] C.J. Batie, H. Kamin, Ferredoxin:NADP+ oxidoreductase. Equilibria in binary and ternary complexes with NADP+ and ferredoxin, J. Biol. Chem. 259 (14) (1984) 8832–8839.

[60] C.J. Batie, H. Kamin, Electron transfer by ferredoxin:NADP+ reductase. Rapid-reaction evidence for participation of a ternary complex, J. Biol. Chem. 259 (19) (1984) 11976–11985.

[61] J.A. Hermoso, T. Mayoral, M. Faro, C. Gomez-Moreno, J. Sanz-Aparicio, M. Medina, Mechanism of coenzyme recognition and binding revealed by crystal structure analysis of ferredoxin-NADP+ reductase complexed with NADP+, J. Mol. Biol. 319 (5) (2002) 1133–1142.

[62] N. Carrillo, E.A. Ceccarelli, Open questions in ferredoxin-NADP+ reductase catalytic mechanism, Eur. J. Biochem. 270 (9) (2003) 1900–1915.
[63] A. Velázquez-Campoy, G. Goñi, J.R. Peregrina, M. Medina, Exact analysis of heterotropic interactions in proteins: characterization of cooperative ligand binding by isothermal titration calorimetry, Biophys. J. 91 (5) (2006) 1887–1904.
[64] M. Martinez-Julvez, M. Medina, A. Velazquez-Campoy, Binding thermodynamics of ferredoxin:NADP(+) reductase: two different protein substrates and one energetics, Biophys. J. 96 (12) (2009) 4966–4975.
[65] M. Medina, C. Gomez-Moreno, Interaction of ferredoxin-NADP(+) reductase with its substrates: optimal interaction for efficient electron transfer, Photosynth. Res. 79 (2) (2004) 113–131.
[66] A.S. López Rivero, M.A. Rossi, E.A. Ceccarelli, D.L. Catalano-Dupuy, A bacterial 2 [4Fe4S] ferredoxin as redox partner of the plastidic-type ferredoxin-NADP, Biochim. Biophys. Acta Gen. Subj. 1863 (4) (2019) 651–660.
[67] Y. Wang, H. Yao, Y. Cheng, S. Lovell, K.P. Battaile, C.R. Midaugh, M. Rivera, Characterization of the bacterioferritin/bacterioferritin associated ferredoxin protein-protein interaction in solution and determination of binding energy hot spots, Biochemistry 54 (40) (2015) 6162–6175.
[68] T.J. Cain, A.T. Smith, Ferric iron reductases and their contribution to unicellular ferrous iron uptake, J. Inorg. Biochem. 218 (2021) 111407.
[69] R. Lill, Function and biogenesis of iron-sulphur proteins, Nature 460 (7257) (2009) 831–838.
[70] J.H. Kim, R.O. Frederick, N.M. Reinen, A.T. Troupis, J.L. Markley, [2Fe-2S]-ferredoxin binds directly to cysteine desulfurase and supplies an electron for iron-sulfur cluster assembly but is displaced by the scaffold protein or bacterial frataxin, J. Am. Chem. Soc. 135 (22) (2013) 8117–8120.
[71] A. Romsang, J. Duang-Nkern, W. Wirathorn, P. Vattanaviboon, S. Mongkolsuk, Pseudomonas aeruginosa IscR-regulated ferredoxin NADP(+) reductase gene (fprB) functions in iron-sulfur cluster biogenesis and multiple stress response, PLoS One 10 (7) (2015) e0134374.
[72] R. Yan, S. Adinolfi, A. Pastore, Ferredoxin, in conjunction with NADPH and ferredoxin-NADP reductase, transfers electrons to the IscS/IscU complex to promote iron-sulfur cluster assembly, Biochim. Biophys. Acta 1854 (9) (2015) 1113–1117.
[73] M.I. González Carreró, F.J. Sangari, J. Agüero, J.M. Garcı, A. Lobo, Brucella abortus strain 2308 produces brucebactin, a highly efficient catecholic siderophore, Microbiology (Read.) 148 (Pt 2) (2002) 353–360.
[74] B.H. Bellaire, P.H. Elzer, S. Hagius, J. Walker, C.L. Baldwin, R.M. Roop, Genetic organization and iron-responsive regulation of the Brucella abortus 2,3-dihydroxybenzoic acid biosynthesis operon, a cluster of genes required for wild-type virulence in pregnant cattle, Infect. Immun. 71 (4) (2003) 1794–1803.
[75] M. Martínez, R.A. Ugalde, M. Almirón, Irr regulates brucebactin and 2,3-dihydroxybenzoic acid biosynthesis, and is implicated in the oxidative stress resistance and intracellular survival of Brucella abortus, Microbiology (Read.) 152 (Pt 9) (2006) 2591–2598.
[76] D. Touati, Iron and oxidative stress in bacteria, Arch. Biochem. Biophys. 373 (1) (2000) 1–6.
[77] P. Cornelis, Q. Wei, S.C. Andrews, T. Vinckx, Iron homeostasis and management of oxidative stress response in bacteria, Metallomics 3 (6) (2011) 540–549.
[78] S.I. Liochev, A. Hausladen, W.F. Beyer, I. Fridovich, NADPH: ferredoxin oxidoreductase acts as a paraquat diaphorase and is a member of the soxRS regulon, Proc. Natl. Acad. Sci. U.S.A. 91 (4) (1994) 1328–1331.
[79] A.R. Krapp, V.B. Tognetti, N. Carrillo, A. Acevedo, The role of ferredoxin-NADP+ reductase in the concerted cell defense against oxidative damage. Studies using Escherichia coli mutants and cloned plant genes, Eur. J. Biochem. 249 (2) (1997) 556–563.
[80] A.R. Krapp, R.E. Rodriguez, H.O. Poli, D.H. Paladini, J.F. Palatnik, N. Carrillo, The flavoenzyme ferredoxin (flavodoxin)-NADP(H) reductase modulates NADP(H) homeostasis during the soxRS response of Escherichia coli, J. Bacteriol. 184 (5) (2002) 1474–1480.
[81] K. Takeda, J. Sato, K. Goto, T. Fujita, T. Watanabe, M. Abo, E. Yoshimura, J. Nakagawa, A. Abe, S. Kawasaki, Y. Niimura, Escherichia coli ferredoxin-NADP+ reductase and oxygen-insensitive nitroreductase are capable of functioning as ferric reductase and of driving the Fenton reaction, Biometals 23 (4) (2010) 727–737.
[82] A.R. Krapp, M.V. Humbert, N. Carrillo, The soxRS response of Escherichia coli can be induced in the absence of oxidative stress and oxygen by modulation of NADPH content, Microbiology 157 (Pt 4) (2011) 957–965.
[83] S. Siedler, G. Schendzielorz, S. Binder, L. Eggeling, S. Bringer, M. Bott, SoxR as a single-cell biosensor for NADPH-consuming enzymes in Escherichia coli, ACS Synth. Biol. 3 (1) (2014) 41–47.
[84] J.A. Imlay, Diagnosing oxidative stress in bacteria: not as easy as you might think, Curr. Opin. Microbiol. 24 (2015) 124–131.
[85] I. Lans, M. Medina, E. Rosta, G. Hummer, M. Garcia-Viloca, J.M. Lluch, À. González-Lafont, Theoretical study of the mechanism of the hydride transfer between ferredoxin-NADP+ reductase and NADP+: the role of Tyr303, J. Am. Chem. Soc. 134 (50) (2012) 20544–20553.
[86] M. Martínez-Júlvez, M. Medina, A. Velázquez-Campoy, Binding thermodynamics of ferredoxin:NADP+ reductase: two different protein substrates and one energetics, Biophys. J. 96 (12) (2009) 4966–4975.
[87] J.K. Hurley, Z. Salamon, T.E. Meyer, J.C. Fitch, M.A. Cusanovich, J.L. Markley, H. Cheng, B. Xia, Y.K. Chae, M. Medina, et al., Amino acid residues in Anabaena ferredoxin crucial to interaction with ferredoxin-NADP+ reductase: site-directed mutagenesis and laser flash photolysis, Biochemistry 32 (36) (1993) 9346–9354.
[88] R. Morales, M.H. Charon, G. Kachalova, L. Serre, M. Medina, C. Gómez-Moreno, M. Frey, A redox-dependent interaction between two electron-transfer partners involved in photosynthesis, EMBO Rep. 1 (3) (2000) 271–276.
[89] M. Medina, R. Abagyan, C. Gómez-Moreno, J. Fernández-Recio, Docking analysis of transient complexes: interaction of ferredoxin-NADP+ reductase with ferredoxin and flavodoxin, Proteins 72 (3) (2008) 848–862.
[90] S. Saen-Oon, I. Cabeza de Vaca, D. Masone, M. Medina, V. Guallar, A theoretical multiscale treatment of protein-protein electron transfer: the ferredoxin/ferredoxin-NADP(+) reductase and flavodoxin/ferredoxin-NADP(+) reductase systems, Biochim. Biophys. Acta 1847 (12) (2015) 1530–1538.